symmetry

MDPI

Article

Study of Behavior of Geometric Symmetries of 3D Objects with Digital Fresnel–Kirchhoff Holograms, Using Non-Redundant Calculations

Joan Manuel Villa-Hernández [1,*], Arturo Olivares-Pérez [1,*], Roxana Herran-Cuspinera [1], José Luis Juárez-Pérez [2], Luis Mancio [1] and Rocío Delesma [1,*]

[1] Optics Department, Instituto Nacional de Astrofisica, Optica y Electrónica, Luis Enrrique Erro No. 1, Santa Maria Tonatzintla, Puebla 72840, Mexico; roxherranc@inaoep.mx (R.H.-C.); luis.mancio@inaoe.mx (L.M.)

[2] Campus Loma Bonita, Universidad del Papaloapan, Av. Ferrocarril S/N, Col Centro, Oaxaca 68400, Mexico; jjuarez65@hotmail.com

* Correspondence: joan.villa@inaoep.mx (J.M.V.-H.); olivares@inaoep.mx (A.O.-P.); rocio.hernandez@inaoep.mx (R.D.)

Abstract: Techniques for producing fast Huygens–Fresnel–Kirchhoff digital holograms using kernel symmetry are studied. This study demonstrates non-linear behavior in computing time, as the sampled area changes with respect to the propagated diffracted area. Given the large amount of data involved in 3D object formation, symmetries are crucial in reducing the computational time. The evaluation of diffraction patterns is implemented to avoid redundant calculations while preserving the precision of the results. This algorithm decreases the required computing time depending on the symmetry of the axes, compared to direct calculation. Interestingly, the reduction in computing time relative to the number of symmetries is not linear. Computing time curves are presented. Some redundant computations are determined by the initial conditions of the object matrix, whether even or odd, along its x and y axes. Diagonal symmetries possess intrinsic redundancy along their axes. The rotation of the image must align with the rotation of the geometric coordinates in each section to ensure accurate calculations.

Keywords: diffraction; Fresnel–Kirchhoff holograms; kernel symmetry; wavefront propagation; computing time reduction

Citation: Villa-Hernández, J.M.; Olivares-Pérez, A.; Herran-Cuspinera, R.; Juárez-Pérez, J.L.; Mancio, L.; Delesma, R. Study of Behavior of Geometric Symmetries of 3D Objects with Digital Fresnel–Kirchhoff Holograms, Using Non-Redundant Calculations. *Symmetry* **2024**, *16*, 1219. https://doi.org/10.3390/sym16091219

Academic Editors: Jing Zhou, Guanhai Li, Xinchao Lu and Yin Xu

Received: 13 June 2024
Revised: 6 August 2024
Accepted: 6 August 2024
Published: 17 September 2024

1. Introduction

Numerical Fresnel holograms employ a Fourier technique with an extra quadratic phase term, with the physical consideration that the object size must be much smaller than the distance between the object and the holographic plane [1].

Different techniques have been described to generate three-dimensional holograms. In the case of an object placed near the focal plane, the three-dimensional object is sampled in different planes of depth, and each plane of the object is multiplied by a quadratic phase factor and Fourier transformed, so that the superposition forms the synthesized hologram [2–8]. Angular spectrum theory provides an approach where the object wave is disassembled in plane waves, each plane wave is multiplied with a phase factor, and the superposition is Fourier transformed [9–13]. Holographic stereograms provide a sequence of perspective views of an object, where each view and their Fourier transform holograms are synthesized by computer and arranged in the viewing order to produce the final composite hologram [14–18]. The last one is the superposition of analytic distributions, where a computer-generated hologram is formed by the superposition of wavefronts emanating from the decomposition of the 3D object's on-line elements [19,20]. Most of these methods use the fast Fourier transform numerical tool for the calculation of the diffraction field, and would greatly benefit from computing time reduction. On the contrary,

numerical Fresnel holograms employ a Fourier technique with an extra quadratic phase term, considering an object size much smaller than the distance between the object and the holographic plane [1]. Recent advancements in computer-generated holography (CGH) have focused on reducing computational complexity and enhancing performance. Methods such as a wavefront-recording plane with a compressed look-up table significantly cut down on calculation time and memory usage [21]. Fast algorithms for line-drawn objects bypass traditional FFT, offering a 56-fold speed increase [22]. Single Fourier transform methods split 3D objects into sub-layers, improving computation speed [23]. Polygon-based CGH has seen state-of-the-art results with new fast analytical methods [24]. Real-time holography benefits from volume representation and improved ray tracing, enhancing depth precision and range [25]. The planar layers method efficiently calculates the far-field patterns of 3D objects [20]. Reviews of CGH algorithms for color dynamic displays address computational and quality challenges [26].

The model developed by Huygens determines the interference pattern by means of a linear superposition of spherical wavefronts emanating from point sources, composing an object and forming a reference wave [27–31]. A full-parallax hologram with 4800×4800 pixels for a 3D object with 966 point sources is computed in 17 min and optically reconstructed [32]. A hybrid approach for occlusion processing in hologram calculation combines point-source and wave-field methods. The 3D scene is layered, with light managed based on point density. The hologram is computed from the nearest layer, avoiding artifacts and outperforming individual methods [33].

Implementing the Fresnel—Kirchhoff diffraction equation and simulating an object formed by a three-dimensional array of point sources, the numerical calculation of the diffraction patterns was carried out first, and the reference wave was added afterwards. While this technique achieves precise results, working in this way results in large amounts of computing time, and reducing these times is of great relevance to the field of study [27–32]. The discrete diffraction equation has to be implemented in such a way as to not include redundancies in the evaluation of the registration plane (2D) [29,30]. This method can be used to simultaneously evaluate symmetrical points in the registration plane, providing these points have equal kernels. As a consequence, when compared to direct calculation, the required computing time is reduced depending on the degree of symmetry, while maintaining the accuracy of results. It was determined that the reduction in the calculation time is not linear between four and eight zones of symmetry. Instead, the time reduction is proportional to the number of points between the objects and propagated field plane. A study is presented, detailing the behavior of computing time between direct calculation, and four and eight symmetry zones of the wavefront propagation of a 3D object, with each of the multilayers using the Fresnel—Kirchhoff diffraction equation.

2. Theory

2.1. Unrestricted Propagator

Huygens describes wavefront propagation by spherical waves as one of the most practical and easy to understand diffraction phenomena [34,35]. Enriched by the mathematical rigor of Fresnel and Kirchhoff, these expressions represent the exact way to calculate the propagation of the diffracted field, as long as the object size is much greater than the working wavelength. Starting with the Fresnel–Kirchhoff diffraction equation and simulating an object consisting of a three-dimensional set of point sources, in a flat area on a point $p(x, y, s)$

$$p(x, y, s) = \iiint O(X, Y, Z) exp(ikr(x, y, s, X, Y, Z)) \frac{cos(\phi)}{r(x, y, s, X, Y, Z)} dXdYdZ, \quad (1)$$

the object $O(X, Y, Z)$ corresponds to an amplitude modulation function, propagated as a complex amplitude at the aforementioned point $p(x, y, s)$. Where $cos(\phi)$ is the obliquity factor, formed by the director cosine, representing the scalar product between $r(x, y, s, X, Y, Z)$ and the unit normal to surface vectors.

As portrayed in Figure 1, $r(x, y, s, X, Y, Z + \Delta Z)$ is the distance vector between the object multilayers and the propagated field plane. Moreover, s is the distance between the object reference plane and the propagated plane, and $p(x, y, s)$ represents the complex wave of the propagated field. The obliquity factor can be expressed as $(s - \Delta Z)/r(x, y, s, X, Y, Z + \Delta Z)$. When working with digital images, Equation (1) takes a discrete form, expressed as:

$$p(x, y, s) = s \sum_{m=1}^{M} \sum_{n=1}^{N} \sum_{q=1}^{Q} O(X_m, Y_n, Z_q) K(x, y, s, X_m, Y_n, Z_q). \tag{2}$$

Each point of $p(x, y, s)$ requires a calculation of $M \cdot N$ spherical waves from the digital image (X_m, Y_n, Z_q). Where the kernel function

$$K(x, y, s, X_m, Y_n, Z_q) = \frac{exp(ikr(x, y, s, X, Y, Z))}{r^2(x, y, s, X, Y, Z)}, \tag{3}$$

is determined by the geometric properties of the pixelized object. This function restricts the spatial frequencies of the complex wave, generated by the $(s - \Delta Z)/r$ obliquity factor, to prevent aliasing in the CGH. Based on the Nyquist-Shannon sampling theorem [36,37], the highest spatial frequency $f_{\max}$ that can be represented with a sampling pitch d is $f_{\max} = 1/2d$. The grating equation links the maximum spatial frequency $f_{\max}$ to the maximum diffraction angle $\phi_{\max}$ with the relation $\sin(\phi_{\max}) = \lambda f_{\max}$. Thus, the area of influence of a point at depth z is defined by its maximum radius $r_{\max}(z)$, such that:

$$r_{max}(z) = \mid z \mid \tan(\phi_{max}) = \mid z \mid \tan(\arcsin(\frac{\lambda}{2d})). \tag{4}$$

The window function K can thus be defined as

$$K(x, y, z, X_m, Y_n, Z_q) = \begin{cases} \sqrt{x^2 + y^2 + z^2} & < r_{max}(z) \\ 0 & otherwise. \end{cases} \tag{5}$$

The Huygens propagation with spherical waves, formally expressed by Fresnel–Kirchhoff, represents the basis of this manuscript because it is the exact expression of the propagated field without restrictions. The crucial part is the position vector r, which corresponds to a modulus of the magnitude of length, determined by the distance between the object and the propagated plane of measurement. A prominent feature of the technique is that the object and the measurement plane are independent in size and sampling, respectively. The drawback of the technique is the computation in propagation by nested shekels, which prolong the computation time; on the other hand, the kernel does not have an inverse transform. For this reason, the reduction in the number of calculations is decisive for the reduction in computing time.

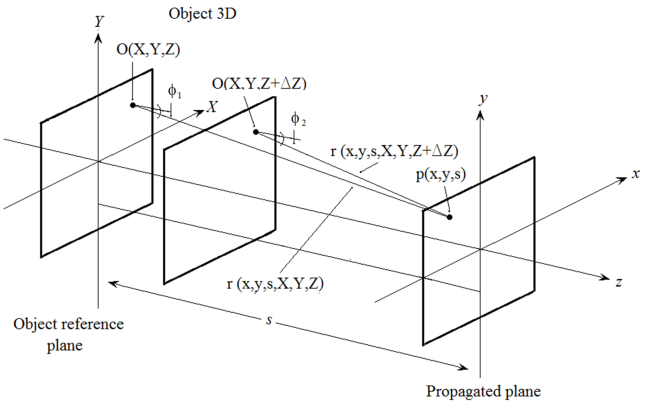

Figure 1. Object represented by two multilayers and their propagation.

2.2. Kaleidoscopic Symmetry

Starting from the Huygens principle, each point of the object corresponds to a spherical wave propagating to the measurement plane of the wavefront. As the object is centered to the wavefront plane, the rectangular and diagonal quadrants satisfy the symmetry. Working within spherical waves, the kernel follows basic geometrical rules. The concept of symmetry can be applied to the kernels of Equation (3).

Rectangular objects have a natural symmetry in the x and y axes, which can divide an object into four equal quadrants. As long as $x = y$, and $x = -y$, they also present a diagonal symmetry. Figure 2 shows a visualization of the diagonals that divide the object into four triangular symmetry zones and the axes into four quadrants.

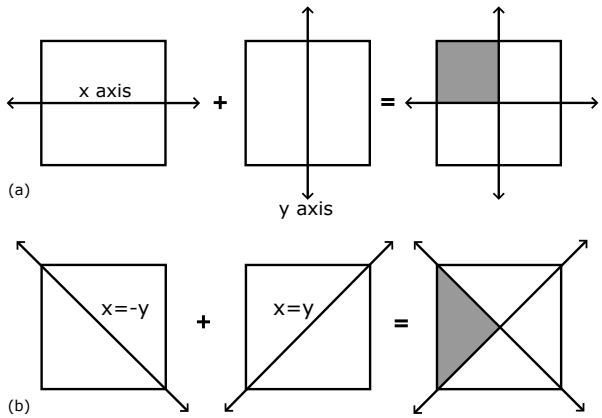

Figure 2. Symmetry zones of the propagated plane: (**a**) Axial divisions along the x-axis and y-axis that combined produce four symmetric quadrants; (**b**) Axial divisions along the lines $x = -y$ and $x = y$ that combined form four symmetric triangular zones. The gray area corresponds to thenon-redundant region of the calculation.

The results of axial and diagonal divisions can be mixed to obtain eight zones of symmetry. Taking advantage of the symmetry, we can adapt an algorithm that uses a fraction of the kernel to calculate it whole. The shaded area in Figures 2 and 3 corresponds to the region where the field is calculated, while the clear areas correspond to the redundancy zone. The concept of kaleidoscope symmetry is based on the symmetry reflections of a small area to sequentially form a whole area. The proposed method results in a significant reduction in computing times when processing the complex wavefront. The kernel obtained is only computed for the gray zone represented. This algorithm decreases the computing time required for the direct computation of Equation (2) and is faster than the four-zone symmetry. When the MN object samples are of considerable size, the difference in computing time between eight- and four-symmetry increases. In turn, the time difference compared to the direct computation also increases.

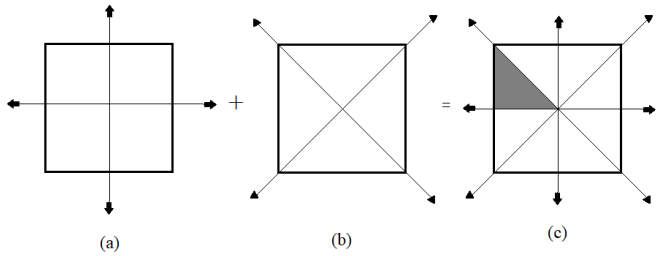

Figure 3. (**a**) Axial symmetry (**b**) Diagonal symmetry (**c**) Kaleidoscopic 8-zone symmetry. The grey area corresponds to the non-redundant region of the calculation.

In essence, the results obtained from the combination of these symmetries open new possibilities for the faster computing of the complex field expressed by Equation (2). Nonetheless, care must be taken when mixing the two symmetries. The centering of the object with respect to the optical axis is an important condition for axial symmetry. To use the diagonal symmetry, we must force our $M \cdot N$ object to $M = N$ by taking the largest value between M or N. These two conditions must be met for an accurate calculation of the complex field using only one eighth of the kernel.

The diagonal and transposition symmetry can be represented by $OT(X_m, Y_n, Z_0) = O(Y_n, X_m, Z_0)$, only the subscripts X_m and Y_n are interchanged; Z_q is an independent value. It is not necessary to change the direction of propagation. The diagonal symmetry when $M \neq N$ is not exact, it is only true for $M = N$. As a general rule, a square with larger size is constructed. For example, the case $M > N$ results in a square matrix of $M \cdot N$, while $M < N$ produces a square of $N \cdot N$. This consideration is an important rule to obtain a correct diagonal symmetry for Equations (6) and (7). Figure 4 shows the images of Figure 3 with $M = N$, with their respective diagonal transformation.

Considering the coordinate axes as lines of symmetry and the object centered with respect to the optical axis, let $O(X_0, Y_0, Z_0)$ be a point in the propagated plane with symmetry points in $O(-X_0, Y_0, Z_0)$, $O(X_0, -Y_0, Z_0)$ and $O(-X_0, -Y_0, Z_0)$. Equation (2) can be represented following the rules of symmetry:

$$
\begin{aligned}
&\textit{Axial} \\
p(x_0, y_0, s) &= s \sum_{m=1}^{M} \sum_{n=1}^{N} \sum_{q=1}^{Q} O(X_m, Y_n, Z_q) K(x, y, s, X_m, Y_n, Z_q) \\
p(-x_0, y_0, s) &= s \sum_{m=1}^{M} \sum_{n=1}^{N} \sum_{q=1}^{Q} O(-X_m, Y_n, Z_q) K(x, y, s, X_m, Y_n, Z_q) \\
p(x_0, -y_0, s) &= s \sum_{m=1}^{M} \sum_{n=1}^{N} \sum_{q=1}^{Q} O(X_m, -Y_n, Z_q) K(x, y, s, X_m, Y_n, Z_q) \\
p(-x_0, -y_0, s) &= s \sum_{m=1}^{M} \sum_{n=1}^{N} \sum_{q=1}^{Q} O(-X_m, -Y_n, Z_q) K(x, y, s, X_m, Y_n, Z_q) \qquad (6) \\
&\textit{Diagonal} \\
p(y_0, x_0, s) &= s \sum_{m=1}^{M} \sum_{n=1}^{N} \sum_{q=1}^{Q} O(Y_m, X_n, Z_q) K(x, y, s, X_m, Y_n, Z_q) \\
p(-y_0, x_0, s) &= s \sum_{m=1}^{M} \sum_{n=1}^{N} \sum_{q=1}^{Q} O(-Y_n, X_m, Z_q) K(x, y, s, X_m, Y_n, Z_q) \\
p(y_0, -x_0, s) &= s \sum_{m=1}^{M} \sum_{n=1}^{N} \sum_{q=1}^{Q} O(Y_n, -X_m, Z_q) K(x, y, s, X_m, Y_n, Z_q) \\
p(-y_0, -x_0, s) &= s \sum_{m=1}^{M} \sum_{n=1}^{N} \sum_{q=1}^{Q} O(-Y_n, -X_m, Z_q) K(x, y, s, X_m, Y_n, Z_q) \qquad (7)
\end{aligned}
$$

An important point is the parameter K which represents the variation in the Z-axis. This parameter is independent of rotation and only follows the position of X_m and Y_n; for each object point, a value of Z_q is associated with it. The Z parameter does not change the direction of propagation.

The four equations in Equation (6) describe the axial transformations, while the four equations in Equation (7) are concerned with the diagonal. In this case, the objects follow diagonal symmetry. Since $O(X_0, Y_0, Z_0)$ is a point in the propagated plane with symmetry points at $O(Y_0, -X_0, Z_0)$, $O(-Y_0, X_0, Z_0)$ and $O(-Y_0, -X_0, Z_0)$, Equation (3) can be represented as follows:

If the size M and N of the object are even, the calculation of the propagated field Equation (2) will have no redundancies in any of the zones. On the contrary, if M is even and N odd, the N axis will have redundancy only in the kernel values at the points within axis. For the case of both M and N being odd, both axes will have redundancies. All redundancy zones can be averaged to obtain the true value of the propagated field in these zones; see Figure A1 in Appendix A.

The kernel Equation (3), $K(x, y, s, X_m, Y_n, Z_q)$ is the same for each symmetry zone; only the object changes its orientation following the rule of signs, as shown in Figure 3. The figure uses flat images with Z_0 constant for the whole set with the orientation of the image samples. A formal demonstration was reported in [29]. The kernel obtained is calculated only for the gray zone represented in Figure 2. This algorithm decreases the computing time required with respect to the direct computation of Equation (2).

Figure 4. Object orientation according to rectangular axial and diagonal symmetries.

The kernel equation (2), $K(x, y, s, X_m, Y_n, Z_q)$ when $M = N$, is the same for each symmetry zone; only the object changes its orientation following the signs transposition rules, as shown in Figure 4. The figure uses flat images with Z_0 constant for the whole set with the orientation of the image samples.

A visualization technique, applied to symmetry using random numbers generated between the values of 0 to 1 and mapped to 256 levels of gray to form a kaleidoscopic pattern, was applied in Figure 5. It shows an eight-zone technique that is used to visualize symmetry through random numbers and form a kind of kaleidoscope. This symmetry is generated with a diagonal section of the first quadrant in Figure 5a), (X_m, Y_n), and then transposed to Figure 5b), of the form (Y_n, X_m), both zones are shown in Figure 5c), and then both are reflected in the $-x$ direction of the form in Figure 5d), $(-X_m, Y_n)$ and $(Y_n, -X_m)$, and the four zones are represented in Figure 5e); these four zones in turn are reflected in the $-y$ direction, Figure 5f), $(X_m, -Y_n)$, $(-Y_n, X_m)$, $(-X_m, -Y_n)$ and $(-Y_n, -X_m)$, where finally the eight zones are shown in Figure 5g), appreciating the symmetrical pattern that forms a kaleidoscope. This pattern assures the correct implementation of the software and the objects, as the calculated field in the specific zones obeys the proposed rules.

For the Fresnel–Kirchhoff field propagator with unconstrained spherical waves, geometric symmetries are described to reduce the calculation area of the measurement plane. The symmetries exposed are those of the coordinate axes, as shown in Figure 2. To make the field correspondent for each symmetrical section, the rotation of the object is used as described in this section. The reduction in area determined by symmetries leads to a lower number of calculations and therefore less computation time.

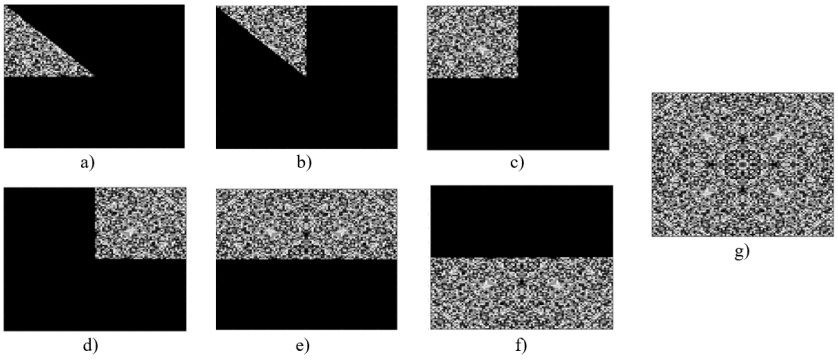

Figure 5. The superposition of axial and diagonal symmetries results in a kaleidoscopic pattern of eight symmetry zones. (**a**) original (grey area, Figure 3), (**b**) transpose, (**c**) sum of (**a**,**b**), (**d**) reflection on the y-axis, (**e**) sum of (**c**,**d**), (**f**) reflection on the x-axis, (**g**) sum of (**e**,**f**).

3. Results

3.1. Computational Results Analysis

The results shown in this work were performed with an Intel (R) Core (TM) i7-7700HQ, Asus, Taiwan, China. @ 2.8GHz processor, taking an average between three different measurements to reduce the effect of variations caused by different factors. At the same time, we worked with randomly generated objects with certain limitations to ensure the generality of the results. The algorithms were prepared with Matlab® software, 2023a.

The algorithm proposed by Equations (2), (3), (6) and (7) are represented by direct calculation and four zones and eight zones, respectively. The results obtained with different programming styles may vary in scale, but it was observed that the trends in the times are maintained.

For the elaboration of the graph in Figure 6, a fixed size wavefront was calculated for a square object with a variable size filled with random information. In this way, we can see how the proposed techniques have a great benefit against direct calculation, especially with large objects. The curvature of the graph can be explained due to the increase in information. As the side of the object increases in size, there is a quadratic growth in the information.

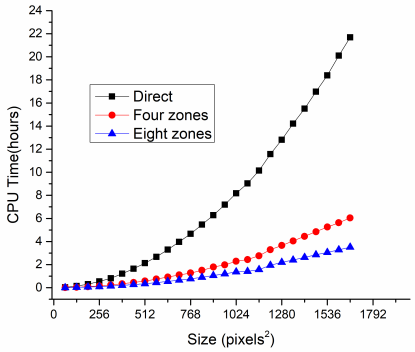

Figure 6. Graph of the computing time required to calculate a 1080 × 1080 wavefront of a square object of different sizes.

As you can see, Figure 6 only reflects the behavior of algorithms against the growth of information, but not on the properties of the object. In other words, with conditions of greater or less symmetry. For this study, two different procedures are proposed to be studied.

In the graph of Figure 7a, an object of variable size was considered, but we kept the same number of points of information. In this particular case, square objects with 10,000 points of information were produced. In this way, it is possible to start with the minimum size necessary to contain this information, obtaining a full object, and therefore,

it can be considered perfectly symmetrical. This situation allows the proposed technique to work under its best conditions, thus obtaining the lowest graph times.

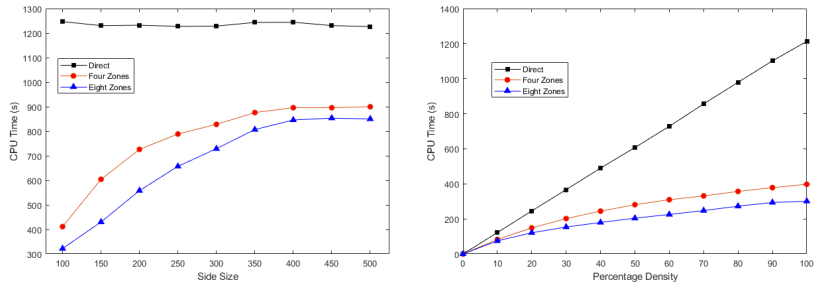

Figure 7. Graphs of the computing time required to calculate a wavefront of objects with different properties, (**a**) A square of variable size with the same number of points inside, (**b**) A square of fixed size whose information density changes.

By increasing the size, the points have more possibilities in terms of location; these were distributed using the Matlab base randomness algorithm, allowing each object to obtain different configurations. It can be seen that the symmetry algorithms are beginning to be less efficient, but better results are maintained compared to the direct process. Continuing with this procedure by increasing the size of the object, a moment will come where the points will be located in asymmetric positions. In the end, a state is reached in which the time no longer changes, since the object has already completely lost its symmetry, with this being the worst condition for the proposed technique.

On the other hand, for the graph in Figure 7b, a similar study is proposed, but in the opposite order. In this case, a square object with a fixed size is prepared, whose information density changes linearly. In the same way, all the information contained was randomly distributed to obtain variable objects.

These results show us that, at the beginning, having little information and therefore little symmetry, the times are very small and the difference between the algorithms is small. At the end of the graph, when having a completely filled or perfectly symmetrical object, the symmetry algorithms differs strongly from the direct one, highlighting its efficiency. In both graphs, the direct calculation reflects the expected behavior; either it remains constant because the amount of information is maintained (Figure 7a) or it grows linearly with the information (Figure 7b).

The symmetries show their non-linear behavior, and for direct calculation it has a quadratic behavior, because it is a function of the area as seen in Figure 6. On the other hand, the use of symmetry of four and eight zones shows another type of non-linear behavior. Figure 7a shows the behavior of the symmetry as a function of the density of points with the same sampling varying the area, observing a constant behavior for direct calculation, which means that it is insensitive to changes in density; however, for the symmetries of four and eight zones it shows a non-linear response, which means that they detect changes in density. In Figure 7b, the change in density occurs by fixing the area and increasing the number of points, observing a linear behavior in the direct calculation, while for the symmetries of four and eight zones they show a non-linear behavior; the three techniques in this way detect changes in density.

Table 1 shows the differences between the different propagators, measured with the same parameters, such as distance and wavelength; the propagation calculation was made directly between the object and the plane of the propagated field for Fresnel–Kirchhoff and Symmetries, while for the angular spectrum propagator and Fresnel, it is necessary to implement a mask, to form a larger matrix where the object is centered and to match the sampling of the propagated plane. On the other hand, a numerical calculation was performed of an object area formed by 100×100 pixels that propagates with a measurement plane with an area of 1000×1000 pixels. With this sampling difference between both

planes, it is necessary to match the samplings in both planes for propagators using Fourier. The working distances of propagators are usually measured with the Fresnel number [38,39]. In propagators that do not use Fourier, the objects can present units of size as in the propagated measurement plane; this value modifies the diffraction pattern in aspects of amplification.

Table 1. Comparison showing different characteristics of the propagators measured with the same parameters.

Conditions	**Propagators**			
	Fresnel Kirchhoff [34,35,39]	**Symmetries [29,30]**	**Angular Spectrum [34,39]**	**Fresnel [34,39]**
Kernel	Spherical wave	Spherical wave	Plane wave	Plane wave
Obliquity angle	yes	yes	no	yes
Object size (D radius)	yes	yes	no	no
Propagated plane size	yes	yes	no	no
z Distance	yes	yes	yes	yes
Working distance range Fresnel Number $F = D^2/(z\lambda)$ [38,39]	$1 \ll F \leq 1$	$1 \ll F \leq 1$	$1 \ll F \leq 1$	$1 \ll F \leq 1$
Spatial frequency limit [36,37] Nyquist—Shannon theorem	$r_{max}(z) = \mid z \mid \tan(\arcsin(\frac{\lambda}{2d}))$	$r_{max}(z) = \mid z \mid \tan(\arcsin(\frac{\lambda}{2d}))$	no	$r_{max}(z) = \mid z \mid \tan(\arcsin(\frac{\lambda}{2d}))$
Computation Time	Very long time	Very long time	Very short time	Very short time
Sampling independence between the object plane and the propagated plane	yes	yes	no	no
Propagation calculation time from 100×100 to 1000×1000 pixels	241.559 s	102.375 s (4-$\mathcal{Z}$) 79.384 s (8-$\mathcal{Z}$)	0.418 s	2.891 s
Matlab Memory Consumption	3457 MB	3110 MB (4-$\mathcal{Z}$) 3410 MB (8-$\mathcal{Z}$)	3376 MB	3350 MB
Mask for window object	no	no	yes	yes
Amplification due to propagation	yes	yes	no	no
Chromatic amplification	yes	yes	yes	yes
Fourier implementation at its core	no	no	yes	yes

3.2. Numerical and Experimental Reconstruction

The usefulness of the proposed method can be confirmed through the optical reconstruction step, with which we can observe a holographic image with a high quality and low signal-to-noise ratio at the holographic plane. Figure 8, shows the numerical reconstructions of various objects and the optical reconstructions. The optical reconstruction were obtained through the use of a spatial light modulator (SLM), by transmission of

1900 × 1080 (HD) 0.74″ diagonal, HD Kit: LCD L3C07U-85G13, bbs bild-u lichtsysteme GmbH, Munich, Germany, which was illuminated with a 530 nm wavelength of laser diode (Figure 9).

Figure 8. Reconstructions of photographs (**a**) Numerical for the direct algorithm, (**b**) Numerical for the four zones algorithm, (**c**) Numerical for the eight zones algorithm, (**d**) Experimental reconstruction with the SLM HD Kit: LCD L3C07U-85G13, using the setup shown in Figure 9.

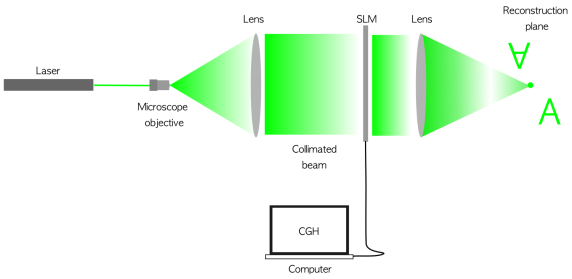

Figure 9. Experimental set up for the reconstruction of CGH. A laser source illuminates a Spatial Light Modulator (SLM) with a plane wave. The SLM is connected to a computer where the CGH is displayed. Using a converging lens, the twin images and the zeroth-order diffraction are reconstructed.

As can be seen, no visual difference is perceived in any of the reconstructions. Therefore, in the experimental reconstruction, no differences are perceived either, so only one is attached in Figure 8. For a more analytical comparison, the correlation between the numerical results of each proposed technique with the direct process is presented.

The reconstruction of the holograms shown in Figures 8 and 10 shows binary images and gray levels. With high quality, these figures also include an experimental reconstruction, where the hologram is shown in a spatial modulator of light, and is reconstructed with a lens that forms a beam of light, converging at a distance where a point image is formed.

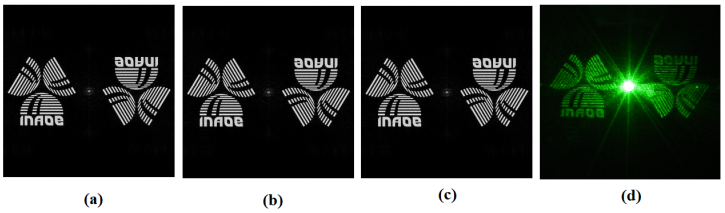

Figure 10. Reconstructions of the INAOE logo (**a**) Numerical for the direct algorithm, (**b**) Numerical for the four zones algorithm, (**c**) Numerical for the eight zones algorithm, (**d**) Experimental reconstruction with the SLM HD Kit: LCD L3C07U-85G13, using the setup shown in Figure 9.

The graphs in Figure 11 show a peak with a maximum correlation of 0.999, at the same time as two small protuberances, due to the double reconstructed image. The graph shows the correlation of the complete reconstructed image of the conjugate pair, as shown in Figure 8. Figure 11a shows the correlation between Figure 8a,b, and Figure 11b shows the correlation between Figure 8a,c. The base of the figures corresponds to the sampling in pixels of the reconstruction plane, and the vertical axis corresponds to the amplitude of the correlation. Color variation is only a visual representative scale.

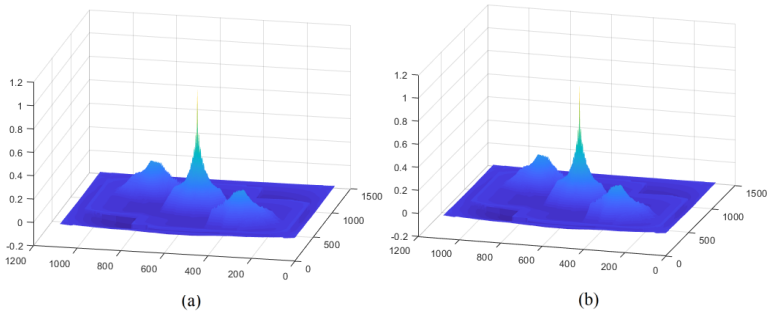

Figure 11. Correlation of the results of the direct algorithm with (**a**) the four zones algorithm and (**b**) the eight zones algorithm.The base area corresponds to the sampling in pixels of the reconstruction plane of Figure 8, and the vertical axis corresponds to the amplitude of the correlation. Color variation is only a visual representative scale.

3.3. Image Composition on Multiple Planes

Figure 12 shows a composition of three images, Fresnel (sourced from [40]), Logo, and Kirchhoff (sourced from [41]), which are located at different distances from the holographic plane; Fresnel at $z_1 = 15$ mm, Logo at $z_2 = 20$ mm, and Kirchhoff at $z_3 = 25$ mm. The size of the image that forms the composition is 1000×1000 pixels, similar to the size of the wavefront where the hologram will be written; the calculation of the wavefront was generated by the eight-zone symmetry technique, where each image is propagated individually and then superimposed to form the composition. The wavelength is $\lambda = 632.8 \times 10^{-6}$ mm.

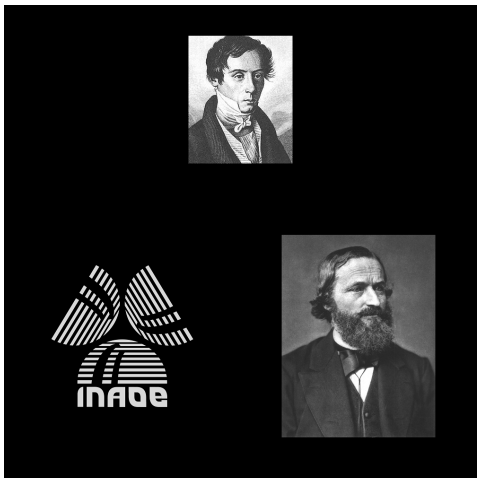

Figure 12. Composition of three images where each image is located at different distances from the holographic plane, Fresnel at $z_1 = 15$ mm, Logo at $z_2 = 20$ mm, Kirchhoff at $z_3 = 25$ mm.

Figure 13 shows the FFT reconstruction, showing only one of the diffracted orders to better visualize the details. In order to correctly focus the object of interest using the FFT, it is necessary to satisfy the lensless Fourier hologram criterion, in which the reference beam has the same distance as the object beam. As shown in Figure 13a, the hologram was reconstructed at distance z_1, obtaining the Fresnel image; in Figure 13b, the hologram is reconstructed at z_2, where the Inaoe logo is shown, and Figure 13c corresponds to z_3 the Kirchhoff image. Figure 13 shows how the diffraction patterns of the objects behave and amplify at different depths of focus. It should be clarified that the hologram can be reconstructed with any arbitrary coherent wavelength; however, for the purposes of focusing each object at the designed distance, the initial wavelength is used, and the Fourier condition is met without lenses [42].

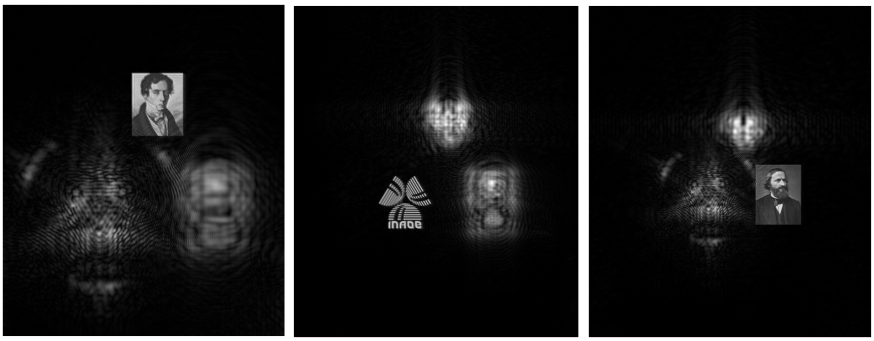

Figure 13. Cropped visualization of the diffracted first order from the reconstruction of the composite holograms, with the Fourier condition without lenses (**a**) focused at the z_1 Fresnel image, (**b**) z_2 Logo image, and (**c**) z_3 Kirchhoff image. Complete spectrum in Appendix B.

The versatility of the technique opens up possibilities for reconstructing objects in different planes, showing their reconstructions at their pre-established distances when their respective wavefronts were constructed.

4. Discussion

Digital Huygens–Fresnel holograms for 3D objects were obtained using the discrete Fresnel-–Kirchhoff diffraction equation, because these data represent the exact values of the propagated field without using an approximation of the kernel, through Fourier with quadratic terms. The proposed technique to compute the diffraction pattern of the object is sufficient to yield excellent digital holograms. Holograms with high precision in the values are necessary for the field of metrology or to quantify physical results obtained through devices with diffractive optics. When reconstructing a diffraction field of the object, it is widely known that calculation times are very high when using traditional methods.

In this study, we show that geometric symmetry techniques for four and eight zones have non-linear behaviors in computing times. Thanks to the different compositions proposed, it could be seen how the algorithm optimization depends directly on the symmetry conditions of the object. Despite this, it was also found that when working with objects of small symmetry, the proposed technique shows an improvement, this being the minimum that can be obtained with this procedure.

The techniques reviewed in this manuscript have great robustness and precision in their calculations, and also require only minimal conditioning to implement symmetries. The symmetries that are used are natural in the scheme of the coordinate system of the Cartesian axes. The implemented math visualizes a reduction in calculation points of the order of four and eight times less than the original calculation. However, computing times do not follow this rule due to the structure of the programming needed to carry out these calculations. The study presented in this document shows these differences. The precision of this technique is very high, when comparing the images of the reconstructed holograms directly, or with the four-zone symmetry algorithm and with the eight-zone symmetry algorithm. Through correlation techniques, this comparison is made. Part of the robustness and simplicity lies in the possibility of rotating the objects, which simplifies the kernel product with the rotated object, giving the equivalence of the calculation to its respective area of symmetry. This point is the essence of the algorithm that we present in this manuscript. The presented technique can be used in conjunction with Look-Up Table (LUT) methods, which have shown significant advances in reducing memory usage [43].

The proposed technique only shows a different way of reducing the calculations using symmetries for the Fresnel–Kirchhoff propagator, which emulates the Huygens concept with spherical waves with their obliquity factor. The obliquity factor helps to visualize the parallax concept of a 3D object, and the point cloud that forms the 3D object is calculated

naturally. The disadvantage of this path is the calculation times, which are very long, as shown in other techniques proposed to calculate the propagated field [27–32]. In some, they use the concept of angular spectrum or Fresnel—both techniques are restricted to the paraxial region—in this case the obliquity factor is removed, and plane waves propagate, no longer fulfilling Huygens' concept. But in return, the fast Fourier transform is implemented directly to the image, and the propagated field is calculated very quickly and efficiently. The deconvolution used in the angular spectrum technique is possible because the Fourier transform has an inverse. The Fresnel–Kirchhoff expression has no inverse, hence the need to use conditioning approximations to calculate it, with adequate and satisfactory results. In display holography, using the proposed technique would be very slow and costly in computational time, but for metrology where field values are very important, it is up to par.

5. Conclusions

Novel methods have been proposed to reduce the computation time in CGH. In this work, the use of four symmetry zones was extended to eight symmetry zones, and it was observed that the reduced time is not linear. The method leveraging symmetrical point evaluation significantly reduces computational time while maintaining accuracy. Additionally, it should be noted that the Fresnel–Kirchhoff has no restrictions regarding the object size relative to the propagation distance. While it faces challenges in computational efficiency compared to other methods employing fast Fourier transforms, its robustness and conditioning requirements make it a viable option for precise field value calculations in metrology. This study underscores the importance of symmetry in algorithm optimization and highlights the trade-offs between computational efficiency and precision in different application domains.

Author Contributions: Conceptualization, J.M.V.-H., A.O.-P. and J.L.J.-P.; Formal analysis, J.M.V.-H., A.O.-P., R.H.-C. and L.M.; Investigation, J.M.V.-H., A.O.-P. and R.H.-C.; Methodology, J.M.V.-H., A.O.-P. and J.L.J.-P.; Project administration, A.O.-P.; Resources, J.M.V.-H., A.O.-P. and R.H.-C.; Supervision, A.O.-P. and R.H.-C.; Validation, J.M.V.-H., A.O.-P. and R.H.-C.; Visualization, J.M.V.-H., A.O.-P. and J.L.J.-P.; Writing – original draft, J.M.V.-H., A.O.-P. and J.L.J.-P.; Writing—review and editing, R.H.-C., L.M. and R.D. All authors have read and agreed to the published version of the manuscript.

Funding: We would also like to extend our gratitude to CONAHCYT, Consejo Nacional de Humanidades Ciencias y Tecnologías, for the financial support given to the students involved in this project.

Data Availability Statement: Data underlying the results presented in this papper are not publicly available at this time but may be obtained from the authors upon resonable request.

Acknowledgments: We are grateful to INAOE, Instituto Nacional de Astrofisíca Óptica y Electrónica, for the equipment and laboratory facilities, as well as for the support with providing supplies.

Conflicts of Interest: The authors declare no conflicts of interest.

Abbreviations

The following abbreviations are used in this manuscript:

FFT	Fast Fourier Transform
SLM	Spatial Light Modulator

Appendix A. Redundancies on Rectangular and Diagonal Axes

Naturally, the axes of symmetry serve as references, but at the same time they are a source of redundancy in the calculation. Figure A1 shows a propagated image, with a matrix $M = N$, odd without prior considerations.

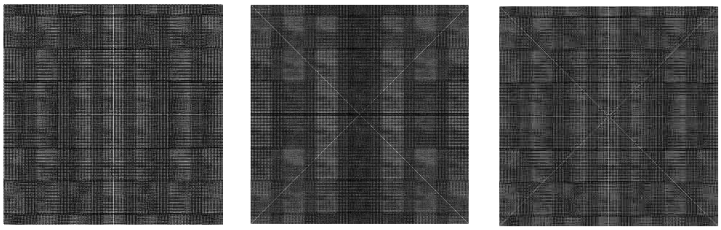

Figure A1. Redundancies in a square form, (**a**) axes symmetries, (**b**) diagonal symmetries, (**c**) redundancies for the eight zones symmetries.

Figure A1 shows the redundancy for a matrix $M \cdot N$ with $M = N$, this condition is essential for the simple use of the symmetry of eight zones. Redundancies on the axes x and y are shown in Figure A1a). A natural way to avoid these is when $M = N$ are even. On the other hand, Figure A1b) shows redundancies on the diagonal axes $x = y$ and $x = -y$. Figure A1c) shows the combination of redundancies. These redundancies are easy to correct, with average point data values in the redundancy zone.

Appendix B. Multiplane Complete Field

Figure A2 shows the reconstruction of a hologram using the fast Fourier transform FFT, where each holographic reconstruction is performed at a given z distance, to obtain the preset images for a z depth, where the conjugated pairs (a), (b) and (c) are displayed. The full spectrum of the conjugate pair, where each element is composed of three images at different depths, for each pair. In Figure 13, only one element of the composite conjugate pair is shown, which corresponds only to the images in the top left. The images correspond to Fresnel with z_1, Logo with z_2, Kirchhoff with z_3. The lower right conjugate pair shows the inverted images. You can also see the behavior of out-of-focus images as a function of the z_1, z_2 and z_3 distances.

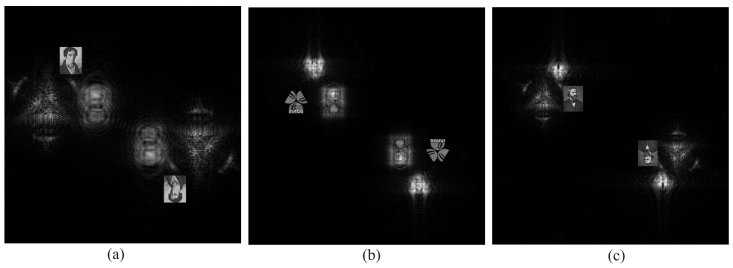

Figure A2. Complete spectrum of the reconstructions shown in Figure 13: (**a**) at distance $z_1 = 15$ from the Fresnel image, (**b**) of the INAOE logo with $z_2 = 20$, and (**c**) Kirchhoff reconstruction with $z_3 = 25$.

References

1. Goodman, J.W. *Introduction to Fourier Optics*, 3rd ed.; Roberts & Co.: Englewood, CO, USA , 2005.
2. Waters, J.P. Three-Dimensional Fourier-Transform Method for Synthesizing Binary Holograms . *J. Opt. Soc. Am.* **1968**, *58*, 1284. [CrossRef]
3. Gerchberg, R.W. A practical algorithm for the determination of phase from image and diffraction plane pictures. *Optik* **1972**, *35*, 237–246.
4. Leseberg, D. Sizable Fresnel-type hologram generated by computer. *J. Opt. Soc. Am. A* **1989**, *6*, 229. [CrossRef]
5. Wakunami, K.; Yamaguchi, M. Calculation for computer generated hologram using ray-sampling plane. *Opt. Express* **2011**, *19*, 9086. [CrossRef]
6. Ying, C.F. New method for the design of a phase-only computer hologram for multiplane reconstruction. *Opt. Eng.* **2011**, *50*, 055802. [CrossRef]
7. Li, F.; Bi, Y.; Wang, H.; Sun, M.; Kong, X. Weighted 3D GS algorithm for image-quality improvement of multi-plane holographic display. *Chin. J. Lasers* **2012**, *39*, 1009001. [CrossRef]

8. Zhou, P.; Li, Y.; Chen, C.P.; Li, X.; Hu, W.; Rong, N.; Yuan, Y.; Liu, S.; Su, Y. Multi-Plane Holographic Display with a Uniform 3D Gerchberg-Saxton Algorithm. *SID Symp. Dig. Tech. Pap.* **2015**, *46*, 442–445. [CrossRef]
9. Leseberg, D.; Frère, C. Computer-generated holograms of 3-D objects composed of tilted planar segments. *Appl. Opt.* **1988**, *27*, 3020. [CrossRef]
10. Leseberg, D. Computer-generated three-dimensional image holograms. *Appl. Opt.* **1992**, *31*, 223. [CrossRef]
11. Jendral, A.; Bräuer, R.; Bryngdahl, O. Synthetic image holograms: Computation and properties. *Opt. Commun.* **1994**, *109*, 47–53. [CrossRef]
12. Yang, H.; Kim, E.S. Waveform-decomposition-based algorithm for horizontal parallax-only-display computer-generated holograms. *Opt. Lett.* **1996**, *21*, 510. [CrossRef] [PubMed]
13. Yang, H.G.; Kim, K.T.; Kim, J.H.; Kim, E.S. 3D digital hologram synthesis based on angular spectrum. In Proceedings of the Aerospace/Defense Sensing and Controls, Orlando, FL, USA, 8 July 1998; pp. 169–178. [CrossRef]
14. DeBitetto, D.J. Holographic Panoramic Stereograms Synthesized from White Light Recordings. *Appl. Opt.* **1969**, *8*, 1740. [CrossRef] [PubMed]
15. McCrickerd, J.T. Comparison of Stereograms: Pinhole, Fly's Eye, and Holographic Types. *J. Opt. Soc. Am.* **1972**, *62*, 64. [CrossRef]
16. Haig, N.D. Three-Dimensional Holograms by Rotational Multiplexing of Two-Dimensional Films. *Appl. Opt.* **1973**, *12*, 419. [CrossRef] [PubMed]
17. Yatagai, T. Three-dimensional displays using computer-generated holograms. *Opt. Commun.* **1974**, *12*, 43–45. [CrossRef]
18. Huff, L.; Fusek, R.L. Color Holographic Stereograms. *Opt. Eng.* **1980**, *19*, 195691. [CrossRef]
19. Leseberg, D. Computer generated holograms: Cylindrical, conical, and helical waves. *Appl. Opt.* **1987**, *26*, 4385. [CrossRef]
20. Bayraktar, M.; Özcan, M. Method to calculate the far field of three-dimensional objects for computer-generated holography. *Appl. Opt.* **2010**, *49*, 4647–4654. [CrossRef]
21. Pi, D.; Liu, J.; Han, Y.; Yu, S.; Xiang, N. Acceleration of computer-generated hologram using wavefront-recording plane and look-up table in three-dimensional holographic display. *Opt. Express* **2020**, *28*, 9833–9841. [CrossRef]
22. Nishitsuji, T.; Shimobaba, T.; Kakue, T.; Ito, T. Fast calculation of computer-generated hologram of line-drawn objects without FFT. *Opt. Express* **2020**, *28*, 15907–15924. [CrossRef]
23. Chang, C.; Zhu, D.; Li, J.; Wang, D.; Xia, J.; Zhang, X. Fast calculation of computer generated hologram based on single Fourier transform for holographic three-dimensional display. *Displays* **2021**, *69*, 102064. [CrossRef]
24. Zhang, Y.; Fan, H.; Wang, F.; Gu, X.; Qian, X.; Poon, T.C. Polygon-based computer-generated holography: A review of fundamentals and recent progress. *Appl. Opt.* **2022**, *61*, B363–B374. [CrossRef] [PubMed]
25. Zhong, C.; Sang, X.; Yan, B.; Li, H.; Chen, D.; Qin, X. Real-time realistic computer-generated hologram with accurate depth precision and a large depth range. *Opt. Express* **2022**, *30*, 40087–40100. [CrossRef] [PubMed]
26. Pi, D.; Liu, J.; Wang, Y. Review of computer-generated hologram algorithms for color dynamic holographic three-dimensional display. *Light Sci. Appl.* **2022**, *11*, 231. [CrossRef]
27. Stein, A.D.; Wang, Z.; Leigh, J.S. Computer-generated holograms: A simplified ray-tracing approach. *Comput. Phys.* **1992**, *6*, 389. [CrossRef]
28. Lucente, M.E. Interactive computation of holograms using a look-up table. *J. Electron. Imaging* **1993**, *2*, 28. [CrossRef]
29. Juárez-Pérez, J.L.; Olivares-Pérez, A.; Berriel-Valdos, L.R. Nonredundant calculations for creating digital Fresnel holograms. *Appl. Opt.* **1997**, *36*, 7437. [CrossRef]
30. Juarez-Perez, J.L.; Olivares-Perez, A.; Gomez-Colin, M.R.; Pinto-Iguanero, B.; Perez-Cortes, M.; Ortiz-Gutierrez, M. Synthesis of digital Fresnel holograms by parallelism of eight points. In Proceedings of the Electronic Imaging, San Jose, CA, USA, 3 June 2002; pp. 258–264. [CrossRef]
31. Zhou, P.; Bi, Y.; Sun, M.; Wang, H.; Li, F.; Qi, Y. Image quality enhancement and computation acceleration of 3D holographic display using a symmetrical 3D GS algorithm. *Appl. Opt.* **2014**, *53*, G209. [CrossRef]
32. Matsushima, K.; Takai, M. Recurrence formulas for fast creation of synthetic three-dimensional holograms. *Appl. Opt.* **2000**, *39*, 6587. [CrossRef]
33. Gilles, A.; Gioia, P.; Cozot, R.; Morin, L. Hybrid approach for fast occlusion processing in computer-generated hologram calculation. *Appl. Opt.* **2016**, *55*, 5459–5470. [CrossRef]
34. Collier, R. *Optical Holography*; Elsevier Science: Saint Louis, MO, USA, 2014.
35. Hariharan, P. *Optical Holography: Principles, Techniques, and Applications*, 2nd ed.; Cambridge Studies in Modern Optics; Cambridge University Press: Cambridge, UK; New York, NY, USA, 1996.
36. Nyquist, H. Certain factors affecting telegraph speed. *Bell Syst. Tech. J.* **1924**, *3*, 324–346. [CrossRef]
37. Shannon, C.E. A mathematical theory of communication. *Bell Syst. Tech. J.* **1948**, *27*, 379–423. [CrossRef]
38. Yao, Y.; Zhang, J.; Zhang, Y.; Bi, Q.; Zhu, J. Off-axis Fresnel numbers in laser systems. *High Power Laser Sci. Eng.* **2014**, *2*, e17. [CrossRef]
39. Born, M.; Wolf, E.; Bhatia, A.B.; Clemmow, P.C.; Gabor, D.; Stokes, A.R.; Taylor, A.M.; Wayman, P.A.; Wilcock, W.L. *Principles of Optics: Electromagnetic Theory of Propagation, Interference and Diffraction of Light*, 7th ed.; Cambridge University Press: Cambridge, UK, 1999.
40. Commons, W. File:Augustin Fresnel.jpg. Wikimedia Commons, the Free Media Repository. 2023. Available online: https://commons.wikimedia.org/w/index.php?title=File:Augustin_Fresnel.jpg&oldid=807443897 (accessed on 3 June 2024).

41. Commons, W. File:Gustav Robert Kirchhoff.jpg. Wikimedia Commons, the Free Media Repository. 2021. Available online: https://commons.wikimedia.org/w/index.php?title=File:Gustav_Robert_Kirchhoff.jpg&oldid=607156280 (accessed on 3 June 2024).
42. Villa-Hernández, J.M.; Olivares-Pérez, A.; Herrán-Cuspinera, R.M.; Vallejo-Mendoza, R. Multiple wavefront manipulation through matrix algebra. *Appl. Phys. B* **2021**, *127*, 15. [CrossRef]
43. Jiao, S.; Zhuang, Z.; Zou, W. Fast computer generated hologram calculation with a mini look-up table incorporated with radial symmetric interpolation. *Opt. Express* **2017**, *25*, 112–123. [CrossRef]